Single cell spatial transcriptomic and translatomic profiling of dopaminergic neurons in health, ageing and disease

Peter Kilfeather[1,2,3#], Jia Hui Khoo[4#], Katherina Wagner[1], Han Liang[4], Maria-Claudia Caiazza[1,2], Yanru An[4], Xingju Zhang[4], Xiaoyan Chen[4], Natalie Connor-Robson[1], Zhouchun Shang[4*] and Richard Wade-Martins[1,2,3,5*]

1. Oxford Parkinson's Disease Centre and Department of Physiology, Anatomy and Genetics, University of Oxford, Dorothy Crowfoot Hodgkin Building, South Parks Road, Oxford, OX1 3QU, UK.
2. Kavli Institute for Nanoscience Discovery, University of Oxford, Dorothy Crowfoot Hodgkin Building, South Parks Road, Oxford, OX1 3QU, UK.
3. Aligning Science Across Parkinson's (ASAP) Collaborative Research Network, Chevy Chase, MD, USA.
4. BGI-Shenzhen, Shenzhen 518083, China
5. Lead contact

#: Joint first authors

*: Corresponding authors:

richard.wade-martins@dpag.ox.ac.uk

shangzhouchun@genomics.cn

Summary

The brain is spatially organized and contains unique cell types, performing diverse functions, and exhibiting differential susceptibility to neurodegeneration. This is exemplified in Parkinson's disease (PD) with the preferential loss of dopamine (DA) neurons of the substantia nigra pars compacta.

Using a PD transgenic model, we conducted a single-cell spatial transcriptomic and DA neuron translatomic analysis of young and old mouse brains. Through the high resolving capacity of single-cell spatial transcriptomics, we provide a deep characterization of the expression features of DA neurons within their spatial context, identifying markers of healthy and aging cells, spanning PD-relevant pathways. We integrate marker enrichment and GWAS data to prioritize putative causative genes for disease investigation; identifying CASR as a novel regulator of DA neuron calcium handling. These datasets (accessible at spatialbrain.org) represent an invaluable resource for the investigation into spatially governed gene expression in brain cells in health, aging and disease.

Introduction

In Parkinson's disease (PD) there is preferential loss of dopaminergic (DA) neurons of the substantia nigra (SN) pars compacta[1,2] and intracellular accumulation of α-synuclein. Age is the biggest risk factor for PD and SN DA neurons may also be lost in healthy aged individuals[3–5]. Overexpression of α-synuclein through locus multiplication causes PD and *in vivo* overexpression of human α-synuclein in the *SNCA*-OVX mouse model recapitulates DA neuron loss[6,7].

Single-cell RNA-sequencing has advanced our understanding of cell-specific expression in complex tissues, such as brain [8–13]. To isolate individual cells, the tissue is dissociated, resulting in destruction of the tissue architecture and gene expression artifacts[14]. Spatial transcriptomics preserves this architecture, however current technologies do not consistently achieve single-cell or subcellular resolution at high throughput[15]. Stereo-seq (spatial enhanced resolution omics-sequencing) offers nanoscale resolution spatial expression data, detecting thousands of genes simultaneously[16].

Single-cell and spatial transcriptomics capture minute quantities of RNA, resulting in lower measurement accuracy compared to bulk RNA-sequencing[17]. Translating ribosome affinity purification (TRAP) enables cell type-specific sequencing with measurement sensitivity comparable to bulk RNA[18–24]. TRAP mRNA is ribosome-bound and engaged in translation, providing a more accurate indicator of protein abundance[25].

In this study, we combined the advantages of Stereo-seq and TRAP to characterize the spatial expression signature of individual cells in mouse brain, with a focus on DA neurons. We developed a protocol to segment single cells from Stereo-seq data and subsequently identified 21 cell types in each brain section. By considering the location of each cell, we identified

genes with spatially variable expression, such as in SN and ventral tegmental area (VTA) DA neurons. By contrasting DA neuron gene expression with other cell types, we identified putative novel markers, including *Slc10a4* and *Cpne7*. Using long-read sequencing of translating mRNA captured by TRAP, we discovered splice variants specific to DA neurons. We further investigated whether DA axons harbor actively translating ribosomes. To aid the investigation of novel causative genes in PD, we demonstrated how measures of expression specificity from Stereo-seq and TRAP can be used to prioritize candidate genes of interest from GWAS regions. By this process, we identified a novel role for *CASR* in regulating intracellular calcium handling in DA neurons. We finally compared aged and young brains, revealing a SN-specific loss of DA neurons and expansion of activated microglia with age. Further, we identified a range of age-related expression changes in DA neurons, spanning multiple PD-relevant pathways.

Results

Integrated transcriptomic profiling in the brain

To combine the advantages of spatial resolution with the sensitivity of the TRAP platform, we generated Rosa26^{fsTRAP} ::DAT^{IREScre} (DAT-TRAP) mice, which express eGFP-L10a in DAT-expressing cells (Figure 1A)[26,27]. DAT-TRAP mice were crossed with *SNCA*-OVX mice and aged to 18 months to investigate the effects of overexpression of human alpha-synuclein and aging on DA neuron gene expression (Figure 1A-B). TRAP samples were prepared from 56 mice, by dissecting the ventral midbrain, dorsal and ventral striatum and incubating each homogenate in paramagnetic beads coated in anti-eGFP antibody (Methods, Figure 1H). Stereo-seq samples were prepared from 7 mice, by cutting 10 µm cryopreserved sections from fresh frozen brains (Methods).

Stereo-seq single-cell spatial transcriptomic profiling enables the identification and annotation of distinct cell types in the brain

To generate *in situ* transcriptomic data, cryopreserved mouse brain sections were mounted onto DNA nanoball-patterned arrays for library preparation. All sections were analyzed as a single group (encompassing both age groups and genotypes) to validate Stereo-seq analysis methodology (Figure 1C, Methods). We produced a spatial map of transcript detection, to visualize the intensity of RNA capture across each brain (Figure 1C). In each map, we observed distinct anatomical compartments and cell boundaries (Figure 1C-D). We developed a custom image processing pipeline to segment individual cells from Stereo-seq brain sections (Figure 1D, Methods and Supplementary Figure 1 for a detailed example). In the first stage, cells were filtered based on the number of detected genes (between 200 and 3000 per cell). We isolated 197,698 high-quality transcriptomes with spatial coordinates from

seven mouse brains. 19,240 genes were detected across all brains, and a median of 903 genes were detected per cell. A summary of the quality control workflow and outcomes is shown in Supplementary Figure 2.

Spatial transcriptomics enables the identification and annotation of distinct cell types using both expression and location features. We divided the entire dataset into training and testing subsets (50/50) and performed unsupervised clustering using expression features (Methods). Twenty-one distinct cell types were identified and could be predicted with robust accuracy in the testing subset (F1 > 0.8, Figure 1E, summary of all identified cell types in Supplementary Table 1). Cell types were labelled according to both their anatomical localization and the genes most distinctively expressed (marker genes). For example, neurons were distinguished from glia by the expression of *Snap25* and by patterned localization in regions, such as the hippocampus or thalamus (Figure 1F-G). Distinct subpopulations of cells could be visualized, such as neurons of the CA1, CA3, dentate gyrus, and subiculum in the hippocampal region, or GABAergic nuclei within the midbrain. Oligodendrocytes, astrocytes, microglia, and erythrocytes were readily identifiable by marker expression (Oligodendrocytes: *Olig1, Mbp, Sox10, Mog*; Astrocytes: *Gfap, Slc1a3, Atp1a2, Mt3*; Microglia: *Tyrobp/Dap12, Ftl1, Cts(a/b/d/f/h/l/s/z), Aif1, Tmem119, Cd68*; Erythrocytes: *Hba- and Hbb- genes*). Mapping the identity of every cell to its spatial position of origin gives confidence in ascribing greater annotation detail than with expression data alone, e.g. labelling CA1 vs CA3 hippocampal neurons.

TRAP generates highly sensitive 'translatomic' profile of dopaminergic neurons

TRAP complements Stereo-seq by generating a highly sensitive measure of gene expression in a target cell type. In addition, mRNA captured by TRAP is engaged in translation, providing a more accurate readout of gene expression, compared to conventional

transcriptomic technologies[25]. For deep characterization of the DA neuron translatome, short- and long-read sequencing were performed on DAT-TRAP samples (Figure 1H). The dissected ventral midbrain and striatum were processed, to enrich for cell body- and putative axon-localized transcripts, respectively. Specific expression of the TRAP transgene was confirmed by immunohistochemical staining for eGFP, which showed distinct colocalization to TH; a marker of DA neurons (Figure 1I). In DAT-TRAP samples, canonical markers of DA neurons were robustly enriched, relative to RNA from bulk tissue homogenate, while markers of other cell types present in the ventral midbrain were depleted (Figure 1J and Supplementary Figure 2D). Principal component analysis (PCA) of DAT-TRAP samples showed a major distinction between DAT-TRAP samples and tissue homogenate samples, indicating the importance of using cell type-specific RNA over bulk 'homogenate' RNA (Supplementary Figure 2E).

Functionally and spatially distinct populations of dopaminergic neurons are detected by single cell spatial transcriptomic profiling

DA neurons are primarily situated in the ventral midbrain and can be separated into SN and VTA populations by their mediolateral position. SN DA neurons are particularly vulnerable to age-related and Parkinsonian degeneration. By spatially resolving each expression profile, DA neuronal analyses could be focused to those most relevant to PD. We sought to identify DA neurons in our Stereo-seq data and to characterize spatially dependent changes in their expression. In total, 2,332 DA neurons were robustly detected across all seven brains (Figure 2A). Canonical marker genes, *Th*, *Slc6a3* (DAT), *Ddc* (Dopa decarboxylase) and *Slc18a2* (VMAT2) were strongly enriched in DA neurons, relative to other cell types (Figure 2B). Highly specific markers were also identified with an underreported role in DA function (e.g. *Slc10a4*, *Cpne7*): *SLC10A4* is a member of the bile acid transporter family and regulates

vesicular uptake of dopamine[28]. *CPNE7* is a calcium-dependent phospholipid binding protein that regulates autophagy and axonal/dendritic extension in other cells[29]. Of the top 100 DA neuron markers identified by Stereo-seq, 98 were also enriched in TRAP samples, confirming the strong concordance of both technologies (Supplementary Figure 3A). The spatial specificity of each marker could be qualitatively confirmed by visualizing the expression of each gene *in situ* (Supplementary Figure 3B-C).

We used the coordinate positions of Stereo-seq DA neurons to identify 142 genes with significant evidence of spatially variable expression (FDR-adjusted $P < 0.01$, Methods). This revealed a gradient of expression aligning with the SN (e.g. *Cplx1*, *Nrip3*) and VTA (e.g. *Calb1*, *Aldh1a1*) of the ventral midbrain (Figure 2C). Genes with spatially variable expression in other brain cell types are reported in Supplementary Table 2. Unsupervised clustering confirmed the presence of two distinct subpopulations of DA neurons, recapitulating the anatomical separation of the SN and VTA (Figure 2D). SN and VTA DA neuronal identity could be reliably predicted in testing data (F1 (SN) = 0.88; F1 (VTA) = 0.83). 533 differentially expressed genes were identified between the two subpopulations (FDR-adjusted $P < 0.05$), including established (VTA: *Calb1*, *Calb2*; SN: *Kcnj6* (*Girk2*), *Cplx1*) and putatively novel markers (SN: *Ndnf*, *Rab3c*, *Rab6b;* VTA: *Ahi1*, *Nnat*). Greater *Sox6* and *Otx2* expression was observed in the SN and VTA, respectively, by determining the number of cells in which each was detected (Supplementary Figure 4). The spatial visualization of cluster assignment and marker gene expression demonstrated that although a SN-VTA distinction is evident, cells from either population can be found in the other brain region. Where possible, the functional study of DA neurons could benefit from stratification of neurons based on the expression of SN-VTA markers.

TRAP reveals the specificity of transcript expression in dopaminergic neurons

To focus on genes actively translated in DA neurons, a measure of gene enrichment was calculated by comparing the abundance of transcripts in DAT-TRAP mRNA and bulk tissue homogenate mRNA. Out of 23,292 genes detected, DAT-TRAP RNA was enriched in transcripts spanning 4,828 genes. This indicated the subset of the transcriptome that is predominantly translated in DA neurons. We next compared DAT-TRAP samples to published TRAP/RiboTag datasets from glutamatergic and GABAergic neurons, astrocytes, microglia, and oligodendrocytes in ventral midbrain. Overall, 2,504 genes were found to be significantly specifically expressed in DA neurons[20,22,30–32], (Methods, FDR-adjusted $P < 0.01$) (Supplementary Figure 3C). We leveraged the combination of short- and long-read sequencing technology to profile the specific splice variants that define DA neurons: 1,617 alternatively spliced genes were detected, relative to ventral midbrain RNA (Supplementary Figure 3E). Interestingly, splicing was not restricted to genes enriched in DAT-TRAP samples: 817 genes demonstrated evidence of differential transcript usage without gene-level enrichment, suggesting that a substantial component of cell type-specific function could be conferred by splicing and not relative gene-level abundance.

We hypothesized that DA axons locally translate mRNA, due to their extensive projection length into the striatum. We used TRAP to capture putative axonal mRNA from the dorsal and ventral striatum (Figure 1H). In striatal DAT-TRAP samples, we observed an enrichment of 1,803 genes (FDR-adjusted $P < 0.01$), including canonical DA markers, *Th* and *Slc6a3* (DAT) (Supplementary Figure 5A). We compared our enrichment data with a previously reported proteomic characterization of the striatal DA axonal compartment and found significant overlap between enriched genes/proteins (Hypergeometric test, $P = 1.71e^{-29}$). The abundance of DA neuron marker genes in striatal DAT-TRAP samples was substantially lower than in midbrain-derived samples, however. We also observed the enrichment of markers of cell types other than DA neurons *(e.g. Gfap, Gad1, Gad2)*. We performed

immunohistochemical staining for TH and GFP in mouse brain sections at the level of the striatum (Supplementary Figure 5B). GFP puncta could be identified that colocalized with TH, however the overall signal was sparse.

Heritability enrichment analysis identifies CASR as a novel regulator of intracellular calcium handling in dopaminergic neurons

Using Stereo-seq and TRAP data, we designed an approach to prioritize candidate genes for sporadic PD investigation. We reasoned that enrichment and specificity measures could be used to partition PD heritability according to causative cell types, as demonstrated previously[33,34]. We measured the cell type-specific enrichment and specificity index (Methods) of genes containing SNPs at an $r^2 > 0.5$ and located within ±1 Mb of 107 common risk variants for sporadic PD[35]. 248 out of 303 genes were considered, after retaining genes with mouse homologs (Supplementary Table 3). We observed a broadly neuronal pattern of candidate gene enrichment in Stereo-seq data (Figure 3A), with SN DA neurons demonstrating the greatest median enrichment. Candidate genes were generally depleted in glial cell types, however *Ctsb, Dpm3, Inpp5f, Rps12, Sbds, Scarb2* and *Stx4a* were commonly enriched between glia and DA neurons (Figure 3A). In TRAP data, DA neurons and oligodendrocytes were jointly found to specifically express the greatest number of candidate genes (Figure 3B). Together, our results indicate a primary role for DA neurons in conferring genetic risk of sporadic PD, however the common enrichment of a minority of genes across distinct cell types also supports cell type-agnostic disease processes, as reported previously[36].

We sought to demonstrate how cell type-specific gene expression could be used to prioritize candidate genes containing variation in linkage disequilibrium with lead PD SNPs. We observed that for 63 out of 91 testable PD GWAS loci, the lead SNP localized to a gene not considered specific or enriched in DAT-TRAP samples. Notable exceptions included

rs356182, rs356203, rs256228, rs5019538 (*SNCA*), rs620513 (*FGF20*), rs11158026 (*GCH1*) and rs649339 (*SYT17*), in which the most proximal gene was also the most significantly enriched and specifically expressed. We focused on risk variant rs55961674, an intronic variant of *KPNA1*. In DAT-TRAP samples, *Kpna1* was depleted and in low abundance, relative to bulk ventral midbrain homogenate RNA, indicating low, nonspecific expression in DA neurons. Three candidate genes within the rs55961674 search window were significantly enriched by TRAP, specifically expressed (compared to other TRAP/RiboTag datasets) and contained variants in linkage disequilibrium with the lead SNP (Figure 3C). *Casr*, encoding the calcium sensing receptor, was selected for further investigation, based on demonstrating the most specific expression to DA neurons.

We first validated specific Casr protein expression in DA neurons of the mouse ventral midbrain (Figure 3D): Intriguingly, we observed a distinctly cytoplasmic pattern of expression specifically in DA neurons, while neighboring cells showed depleted cytoplasmic signal and intense nuclear staining. To confirm this difference, we compared the ratio of cytoplasmic to nuclear Casr intensity and found significantly higher cytoplasmic expression in TH-positive than TH-negative cells of the ventral midbrain (Figure 3D, Methods).

We next sought to investigate CASR expression and function in human pluripotent stem cell (iPSC)-derived DA neurons. We observed that CASR protein was prominently expressed in TH-positive neurons, with a diffuse cytoplasmic signal (Figure 3E). To evaluate whether CASR protein was functional and able to modulate intracellular calcium levels and dynamics in iPSC-derived DA neurons generated from a Parkinson's patient carrying an *SNCA* triplication mutation, we measured cytoplasmic calcium in cells treated for one hour with R568 (10 μM), a positive allosteric modulator of CASR[37]. To estimate the levels of calcium stored in the intracellular compartments, we stimulated the cells with ionomycin (5 μM) and

measured the increase in cytoplasmatic calcium using Fura-2AM[38]. The ionomycin-evoked calcium release in the cytoplasm was significantly increased in the iPSC-derived DA neurons from Parkinson's patients and controls acutely treated with R568 (Figure 3F).

By integrating expression specificity data, GWAS summary statistics and the ability to functionally study gene function in iPSC-derived DA models, we can identify genes with novel function with a putative disease role in DA neurons.

Stereo-seq captures the loss of nigral dopaminergic neurons and a neuroinflammatory expansion of microglia with age

Age remains the most important risk factor for neurodegeneration. We therefore sought to assess aging-related changes in cell number, by comparing the abundance of annotated spatial cell types between old and young brains (Figure 4A). SN DA neurons were most significantly depleted (FDR-adjusted $P = 8.01e^{-7}$), while an activated population of microglia and oligodendrocytes were most significantly enriched (FDR-adjusted $P = 1.37e^{-8}$ and $1.\ 37e^{-6}$ respectively). The expansion of activated microglia in aged brains was restricted to the midbrain, corpus callosum and external capsule (Figure 4B). Immunohistochemical staining for Tyrobp/Dap12 (the most enriched Stereo-seq-derived marker of this microglial population), confirmed an increase in the number of Tyrobp/Dap12-positive cells with a microglial morphology (Figure 4B).

We next tested for differential gene expression between aged groups in each cell type (Figure 4C). Glial cell types exhibited a more pronounced aging expression change, with 50 genes found to be significantly differentially expressed, compared to 20 in neurons (FDR-adjusted $P < 0.05$). Furthermore, the absolute magnitude of changes was greater in glia (median absolute $\log_2$ fold change: glia, 0.183; neurons, 0.0991). Ribosome-related genes (*Apod*,

Rpl13a, Rps17, Rpl34, Rps21, Rpl37a) were upregulated, in agreement with previous studies of aging changes in brain[8]. Additional glial changes included a reduction in the expression of myelin sheath components (*Mal, Mbp*), and an increase in the expression of scaffolding-related genes (*Kif5a, Dynll1, Hsp90aa1*).

Expression changes between control and *SNCA*-OVX mice at young and old timepoints (analyzed both together and separately) were subtle. In TRAP samples, overexpression of *SNCA* could be confirmed, on a background of normal *Snca* abundance (Supplementary Figure 5C). No other genes were identified as significantly differentially expressed in DA neurons between control and *SNCA*-OVX by TRAP. Stereo-seq revealed differential expression of 39 genes spanning 9 other cell types in *SNCA*-OVX brains, across both age groups (FDR-adjusted $P < 0.05$), including cortical and midbrain neurons (Supplementary Figure 5D). Many of these genes have previously reported roles in PD pathology, including *Ywhah, Psap, Rtn4,* and *Cst3*.

TRAP reveals the extent of age-induced expression changes in dopaminergic neurons

We used TRAP to provide a deeper focus on DA neuron differential gene expression with aging. Greater measurement sensitivity and cohort size led to the discovery of 667 genes with altered expression in aged TRAP samples (399 upregulated, 268 downregulated, FDR-adjusted $P < 0.01$) (Figure 4D). Thirteen candidate PD GWAS genes were among the differentially expressed genes, including *Gpnmb*, also found to be enriched in both DA neurons and oligodendrocytes, and in agreement with previous age-related neuronal findings[8]. We used 1,931 high-confidence protein-protein interactions to subdivide differentially expressed genes into functionally related clusters (Figure 4E, Methods). Each cluster of genes was distinctly enriched for terms related to neuronal function, with particular

importance in PD (e.g. Lysosomal V-ATPase activity, locomotory behavior and synaptic endocytosis). By taking the directionality of expression change into account, gene set enrichment analysis further indicated an upregulation of synaptic and lysosomal-related genes (e.g. *Syt1, Syt11, Sv2a, Ap2b1, Atp6v0a1, Atp6v0d1, Atp6v1e1, and Atp6ap1*) and a downregulation of mitochondrial and PD-related genes (*mt-Co1, mt-Nd1, mt-Nd4, mt-Nd5, mt-Cyb*).

Discussion

In this study, we generated a single cell-level spatial transcriptomic map of gene expression in the adult mouse brain and produced a high-fidelity translatome-level profile of DA neuron gene expression. By integrating these two data modalities, we characterized the distinctive expression features of DA neurons, demonstrated how expression specificity can be used to prioritize candidate causal genes in PD, and examined the changes that occur in the brain and DA neurons specifically with age.

We identified 21 distinct cell types by unsupervised clustering of cells, based on their expression properties. The spatial compartmentalization of distinct cell types could be mapped to anatomical regions, as in the case of neuronal populations of the hippocampus, thalamus, and midbrain. The ability to spatially visualize each cluster aided the annotation of cell types, however as methods of spatial transcriptomic analysis develop, we anticipate the integration of spatial information directly into the clustering process, wherein cells with close spatial proximity or patterned localization (e.g. cortical, intestinal and dermal layers) and matched expression are more considered more similar.

The capture area of each Stereo-seq array is 100 mm^2 in this study; larger than existing available spatial transcriptomic technologies (Visium, 42.25 mm^2; Slide-Seq 7.1 mm^2)[39–41], and each Stereo-seq array contains 40 billion capture spots (Visium, 5,000; Slide-Seq, tens of thousands). We leveraged this greater size and density of information to spatially resolve individual cells across the brain. By achieving nanoscale resolution, single-cell spatial data were generated without the need for deconvolution-based methods. We also did not require matched single-cell RNA-seq samples for cell identity annotation.

By integrating Stereo-seq and TRAP data, we identified the expression features most specific to DA neurons in comparison to neighboring cell types. While Stereo-seq provided spatial context, single-cell resolution, and a greater number of unique cell types for comparison, TRAP demonstrated greater measurement sensitivity. By integrating short- and long-read sequencing data from TRAP RNA, we have been able to profile the state of splicing in DA neurons, revealing differential transcript usage across more than a thousand genes. We detected 817 instances of alternative splicing in which individual isoforms were enriched by TRAP, but the overall gene-level count was not. This finding indicates that mouse DA neurons actively translate a larger number of genes than are detectable from only gene-level count data. Our understanding of cell type-specific expression is strengthened by considering transcript-level expression data.

The single-cell resolution of Stereo-seq enabled the distinction of SN and VTA DA neurons in ventral midbrain. Although we detected subtypes within both populations, we have not reported them here, as their identity could not be accurately predicted by gene expression in testing data, according to our stringent F1 score requirement. We expect the addition of

further Stereo-seq samples, coupled with improved spatial clustering method development will lead to the robust identification of further DA neuron subtypes in our data.

We used measures of expression specificity from Stereo-seq and TRAP to demonstrate how genes within disease risk loci can be prioritized for investigation. We showed that candidate causal gene expression was most specific to SN DA neurons, supporting the hypothesis that selective vulnerability may be in part conferred by the selective expression of causative genes[33]. We focused on a window surrounding rs55961674 for study, as this SNP falls within the intronic region of *KPNA1*; a gene considered to not be expressed abundantly or with specificity in DA neurons. By leveraging the sensitivity of TRAP and the diversity of cell types detected in Stereo-seq, we could rank linkage-associated genes surrounding rs55961674 by their expression specificity. The specificity of cytoplasmic *Casr* expression to DA neurons and demonstration of its functional role in regulating intracellular calcium handling indicates that variation in this gene could contribute to PD disease risk. Long-term functional study of this gene is of interest, such as by generating a DA neuron-selective knockout *Casr* mouse model.

The large capture area of the Stereo-seq array, combined with single cell-level resolution, enabled parallel region-dependent and cell type-dependent comparison. We identified an age-dependent reduction in SN DA neuron cell number. This supports previous findings that DA neuron number declines with age[1,2] and demonstrates the ability of Stereo-seq to identify a subtype of DA neuron that is most vulnerable to aging. In addition, we detected and confirmed the expansion of microglia with age, expressing a variety of pro-inflammatory markers. Previous investigations into changes in microglial number with age have reported disparate findings, depending on the species and brain region investigated[8,42,43]. However,

age-related neuroinflammation has been shown previously to significantly contribute to degeneration in PD[44].

A surprising finding in this study was the absence of detectable gene expression changes due to *SNCA* overexpression. The age-dependent pattern of SN DA neuronal loss in *SNCA*-OVX mice is considered to recapitulate the slow progression of PD pathology in patients. We would suggest that the transcriptional effects of *SNCA* overexpression (at the level achieved by the *SNCA*-OVX model) are subtle. To capture the gene expression changes induced by the interaction of *SNCA* overexpression and aging, it may be necessary to sample a greater number of timepoints and replicates. In addition, the *SNCA*-OVX mice used in this study also expressed *Snca* (Methods). The expression of wild-type *Snca* may ameliorate disease-related pathology previously observed in *Snca*$^{-/-}$ *SNCA*-OVX mice.

We leveraged the sensitivity of TRAP to assess the evidence for axonal translation in DA neurons. We observed enrichment of DA markers, *Th, Slc6a3 (DAT), and Slc18a2 (VMAT2)* in striatal TRAP samples, however we also observed enrichment of markers of other cell types. Furthermore, the abundance of DA markers in striatal TRAP samples was markedly lower than in midbrain-derived samples. We detected GFP puncta in striatum that colocalized with TH, although overall signal was sparse.

Hobson et al. previously used RiboTag, a similar technology to TRAP, to study axonal translation in DA neurons and concluded that there was no evidence for the process occurring. We conclude that we do see evidence for axonal translation in DA neurons by TRAP, although we suggest that the scale of activity is substantially lower than at the level of the cell body. The enrichment of markers of other cell types in striatal TRAP samples also

indicates the likelihood of low-level ectopic expression of the eGFP-L10a transgene in neighboring cells, as has been reported in DAT-Cre lines[45].

An ongoing challenge for droplet-based single cell and emerging spatial transcriptomic technologies will be to increase the sensitivity of gene detection. Lower detection sensitivity leads to zero inflation, in which many genes are detected at the population level but are largely undetectable at the individual cell level[46,47]. The power to detected differential expression is limited by zero inflation. Lateral diffusion of RNA also limits the resolving capacity of current spatial transcriptomic methods[48]. To minimize the impact of diffusion, we segmented individual cells by spatial read intensity, excluding lower intensity background regions. In addition, we excluded all cells that co-expressed markers of neurons and glia. TRAP demonstrated greater detection power (over 15,000 genes per sample), offering the most inclusive and sensitive measure of DA gene expression currently available. The limitation of TRAP is its specificity to cell subpopulations. DA neurons of the SN and VTA could not be reliably separated during tissue processing due to their close proximity, so measurements reflect the averaged expression of these regions. With greater detection sensitivity and/or sample number, further DA neuron subpopulations may become identifiable.

Together, our spatial transcriptomic and translatome profiling of DA neurons represent a valuable resource to the neuroscience community. Our spatial data can be used to prioritize candidate causal genes involved in conferring genetic risk of brain-related diseases other than PD. In addition, these data can be used as a reference for the development of novel analytical approaches to spatial research. Our TRAP data provides a reference for the querying of genes

or isoforms specific to DA neurons in health and with age. We have combined all results from analyses in this study into a database for public access: *spatialbrain.org*

Methods

Ethics statement and animal husbandry of Mus musculus

All experiments and procedures conducted on animals were carried out in accordance with United Kingdom Home Office regulations under the Animal (Scientific Procedures) Act (1986), and were approved by the local ethical review board of the Department of Physiology, Anatomy and Genetics at the University of Oxford. All mice were housed in the University of Oxford Biomedical Services Building. Mice had access to standard food and water ad libitum. Mouse holding rooms were maintained at 22 °C and 60 to 70% humidity on a 12-hour light-dark cycle. All mice were bred on a C57/BL6 background (MGI Cat# 2159769, RRID:MGI:2159769). For all experiments, animals of both sexes were used unless indicated otherwise.

Transgenic model generation

Homozygous Rosa26^{fsTRAP} mice were bred with homozygous DAT^{IREScre} mice to generate heterozygous Rosa26^{fsTRAP}::DAT^{IREScre} offspring that were used for TRAP experiments. Rosa26^{fsTRAP} parents were crossed and bred to be hemizygous *hSNCA*+ (*SNCA*-OVX): Offspring were a mixture of hemizygous *hSNCA*+ and *hSNCA*-. All animals were wild-type mouse *Snca*$^{+/+}$, due to the position of the ROSA26- eGFP-L10a locus being on the same chromosome as *Snca* (chromosome 6). Routine ear-clipping, digestion and PCR-genotyping was performed as described in Hunn et al[7]. Primer sequences used for confirmation of transgene expression are supplied below[6,7,26,27].

Table 1: Primer sequences for mouse genotyping

Primer	**Forward**	**Reverse**
Wild-type ROSA26 Locus	AAGGGAGCTGCAGTGGAGTA	CCGAAAATCTGTGGGAAGTC
ROSA26-eGFP-L10a	AAGGGAGCTGCAGTGGAGTA	CGGGCCATTTACCGTAAGTTAT
eGFP-L10a 1	TATCATGGCCGACAAGCAGA	CACCGTCTCCAGAAACTTGC
eGFP-L10a 2a	CAAAGACCCCAACGAGAAGC	CTCCACCGTCTCCAGAAACT
eGFP-L10a 2b	CAAAGACCCCAACGAGAAGC	TTGGCTTCATCACAGTGCTG
DAT Wild-type	TGGCTGTTGGTGTAAAGTGG	GGACAGGGACATGGTTGACT
DAT-Cre	CCGGGCTGCCACGACCAA	GGCGCGGCAACACCATTTTT
SNCA-OVX 3′ BAC Junction	GGCCTCTGTCGTTTCCTTTCTCTG	ACGTGCATAGGCAGAGCTAAAACT
SNCA-OVX 5′ BAC Junction	CACTGAGTATTGTTCTGGTAAC	TCAAACATGAGAATTGGTCG

TRAP

Mice were sacrificed by cervical dislocation, the ventral midbrain and striatal tissue were rapidly dissected and affinity purification of eGFP-tagged polysomes was performed as previously described[18]. Briefly, dissected tissue was immediately dounce homogenized in lysis buffer containing 20 mM HEPES KOH, 150 mM KCl, 10 mM MgCl2, 0.5 mM DTT, 100 µg/mL cycloheximide, RNasin (Promega) and SUPERase-in (Life Technologies) and Complete-EDTA-free protease inhibitors (Roche) in Rnase-free water. The lysate was cleared by two-stage centrifugation for 10 minutes at 2,000 x *g* and 20,000 x *g*. Each lysate was incubated with monoclonal anti-GFP antibodies (Heintz Lab; Rockefeller University Cat# Htz-GFP-19C8 and Htz-GFP-19F7, RRID:AB_2716737 and RRID:AB_2716736), coated on paramagnetic beads through a streptavidin-biotin-protein L linker (Pierce; Thermo Fisher Scientific) for 18 hours at 4°C. To remove non-specifically bound material, including RNA, beads were washed 6 times in a high-salt solution containing 20 mM HEPES KOH (pH 7.4), 350 mM KCl, 10 mM MgCl2, 1% NP-40, 0.5 mM DTT, 100 g/ml cycloheximide, and Rnasin and Superasin. RNA was extracted using the Rneasy Micro Plus kit (Qiagen). RNA quantity

and integrity were measured using the Quant-it™ RiboGreen RNA Assay Kit (Thermo Fisher) and Agilent 2100 Bioanalyzer, respectively.

Long-read sequencing and data processing

Twelve TRAP samples were sequenced using the Oxford Nanopore Technologies MinION platform. TRAP samples were equally divided by age and genotype (N = 3 per age:genotype). Library preparation was performed using the cDNA-PCR kit (SQK-PCS109). Raw fast5 data was basecalled and demultiplexed using Guppy (v4.5.2). Read data from FASTQ files were aligned to the mm10 genome (Gencode M25 GRCm38.p6) using minimap2 (v2.18, RRID:SCR_018550)[49]. Transcript level quantification was then performed using Salmon (v1.4.0, RRID:SCR_017036)[50].

Stereo-seq library preparation and sequencing

Stereo-seq libraries were prepared as previously described by Chen *et al*. (2022). In brief, Stereo-seq samples were first prepared by collecting postmortem mouse brains and flash-freezing at -80°C. 10 μm tissue sections were collected -3.5 mm from bregma using a Leica CM1950 cryostat and adhered to each Stereo-seq chip (BGI Research). The chip was placed on a warming plate at 37°C for 3 minutes and fixed in methanol at -20°C for 30 min. The chip was incubated with 100 μL 0.1 % pepsin at 37°C for 12 min for permeabilization and washed with 0.1× SSC buffer containing 0.05 U/μL RNase inhibitor. RNA captured by the DNA nanoball on the chip was reverse transcribed at 42°C for 90 min. Tissue was removed from the chip by incubating with tissue removal buffer at 55°C for 10 min. After washing with 0.1× SSC buffer, the chip with cDNA was incubated with 400 μL cDNA release buffer at 55°C for 4 hours. cDNA was purified and amplified using cDNA primer. A total of 20 ng of cDNA was fragmented, amplified, and purified to generate each cDNA sequencing library.

The cDNA library was sequenced on a MGI DNBSEQ-Tx sequencer with the read length of 50 bp for read 1 and 100 bp for read 2.

Immunohistochemistry

Mice were anaesthetized by intraperitoneal injection of 150 µl pentobarbital. Upon loss of the pedal withdrawal reflex, the thoracic cavity was opened, and 25 mL of phosphate-buffered saline (PBS) was administered transcardially, followed by 25 mL of 4% paraformaldehyde (PFA), diluted in PBS. The brain was extracted and stored overnight in 4% PFA at 4 °C. Brain tissue was next dehydrated, and paraffin embedded through graded alcohols, histoclear (ThermoFisher Scientific) and paraffin solution. Tissue blocks were finally sectioned at 7 µm using a Leica microtome (Leica Microsystems, Wetzlar, Germany) and mounted on glass slides (VWR, Superfrost® Plus).

Sections were prepared for immunofluorescence by performing dewaxing in histoclear, rehydration in graded alcohols, antigen retrieval by microwave heat (20 min) and citrate buffer (ab96678, Abcam). Tissue was blocked for 1 hour at room temperature using 10% donkey serum in TBS. Primary antibodies to TH (Abcam Cat# ab76442, RRID:AB_1524535, 1:500), GFP (Thermo Fisher Scientific Cat# A-11122, RRID:AB_221569, Invitrogen, 1:1000), CASR (Abcam Cat# ab79038, RRID:AB_2071489, 1:100) and TYROBP/DAP12 (Abcam Cat# ab283679, 1:100) were prepared in blocking solution and incubated overnight at 4 °C. Slides were washed using TBS and incubated in secondary antibodies (Alexa Fluor-conjugated anti-rabbit/sheep 1:1000) and DAPI (Thermo Fisher Scientific Cat# D3571, RRID:AB_2307445, 1:5000) for 1 hour at room temperature. Slides were washed and coverslips mounted using FluorSave mounting medium (Millipore, Massachusetts, United States of America).

For detection and quantification of Tyrobp/Dap12-positive cells and analysis of Casr-positivity, two custom pipelines were built using CellProfiler, provided in the accompanying GitHub repository to this manuscript[51]. To calculate the Casr cytoplasm:nucleus ratio, a 10 pixel-wide cytoplasmic object was created, originating from each DAPI-positive spot (nucleus). Each nucleus and cytoplasm was classified either as TH-positive or TH-negative, based on overlapping cytoplasmic TH signal. Objects with only partial TH overlap were filtered, to ensure accurate classification. The maximal Casr intensity for each object was recorded and summarized for each mouse by calculating the mean across objects. The Casr cytoplasm:nucleus ratio represents the ratio of these means.

Immunocytochemistry

After R568 treatment, the iPSC derived neurons were fixed in 4% PFA. Cells were permeabilized for 10 min a solution of 5% NDS, 1% BSA and 0.5% Triton-X 100. Samples were blocked in a solution of 5% NDS and 1% BSA for 1 h. Cells were then incubated for 16 h O/N at 4°C with the following primary antibodies: CASR (Abcam Cat# ab79038, RRID:AB_2071489, 1:500), MAP2 (Abcam Cat# ab92434, RRID:AB_2138147, 1:1000), tyrosine hydroxylase (Millipore Cat# AB1542, RRID:AB_90755, 1:500). Cells were washed twice in PBS and then incubated in secondary antibodies and DAPI for 1.5 h at RT. Cells were washed 3 times and stored in fresh PBS until imaging. Cells were imaged using the OperaPhenix (PerkinElmer).

Fura-2

Fura-2 AM was prepared to 5 mM concentration in calcium-free HBSS supplemented with 20 mM HEPES. It was then diluted to the final concentration of 2.5 mM in Neurobasal

medium supplemented with B27 and L-glutamine, with DMSO (0.1%) or the CaSR positive modulator R568 (10 μM).

iPSC-derived DAns were incubated in the solution of Fura-2 AM and drug for 1 h at 37°C, 5% CO_2 and then imaged on a FlexStation 3 Multi-Mode Microplate Reader (Molecular Devices) at 37°C. The dye was excited at 340 nm and 380 nm and was detected at 510 nm. Each well was imaged every 4 s for 100 s and injected with ionomycin (final concentration 5 μM) after a baseline of 28 s.

For the analysis, the 340/380 ratio was computed, and then the baseline was subtracted from all the timepoints, to obtain a normalized trace for each well. The maximum intensity (peak amplitude) of the normalized trace was found and the area under the curve (AUC) was calculated using the left rectangular approximation method.

Processing of raw Stereo-seq data, quality control and cell type identification

Raw gene-by-spot data per sample were aggregated to create a 2-dimensional image of RNA signal for each sample using custom Python (v3.9.0, RRID:SCR_008394) scripts (Supplementary Materials). To segment individual cells, each image was subjected to a processing pipeline written in Fiji (v1.53q, RRID:SCR_002285) (workflow illustrated in Supplementary Figure 1). Steps taken: Gaussian filter (sigma = 5), background subtraction (rolling ball, 100 pixels), iterative intermeans thresholding, conversion to mask, fill holes, watershed, invert LUT and finally each cell was labelled using the label function in SciPy (v1.9.0, RRID:SCR_008058). Raw gene-by-spot data were then aggregated to the gene-by-cell level and imported into scanpy (v1.9.1, RRID:SCR_018139)[52].

The initial Stereo-seq dataset contained 374,841 cells. In a first round of filtering, low complexity and putative doublet/triplet cells were filtered. To remove low complexity cells, a minimum gene detection cutoff of 200 was selected. To remove putative doublet/triplet cells,

a maximum gene detection cutoff of 300 was selected. After first round filtering, 253,270 cells remained. Count data were log transformed and normalized using a Python implementation of SCTransform[53].

A uniform manifold projection (UMAP) was generated for cells from each mouse brain and overlaid, showing a similar pattern of separation. Count data were therefore concatenated into a single expression object, without additional batch correction or integration methods.

For cell type identification, Leiden clustering was performed at iteratively greater resolutions[54]. At each resolution, a logistic regression model was fitted on a training subset of data (50 %). The ability to predict cluster identity within the testing subset (50 %) was assessed by F1-score. Clusters that could be predicted with an F1-score ≥ 0.8 were considered for further subclustering. Clusters that could not be predicted accurately ($F1 < 0.8$) were discarded and the identity of included cells was annotated as the parent cluster. If a cluster contained fewer than 200 cells, it was considered final and no further subclustering was performed.

Marker genes for each cluster were identified using both the Wilcoxon rank-sum test and MAST mixed-effect hurdle model, providing two-sided *P* values. The identity of each cell type was annotated by integrating marker gene data with previous literature and by confirming the spatial distribution of clustered cells.

A second round of cell filtering was performed after clustering to remove cells that were enriched in both *Snap25* and *Plp1*. We suspected that these cells represent neuronal/glial contaminated mixtures, as previously reported in single cell data[55]. After second-round filtering, 197,698 cells remained.

Spatially variable gene detection

Spatially variable genes were identified using SpatialDE2 with default settings. Coordinates and full expression matrices of each brain were supplied, divided by cell type. To combine results from separate samples, a meta-analysis was performed on the raw *P* values from each sample, using Fisher's method. The Benjamini & Hochberg correction for multiple comparisons was subsequently used and genes were considered spatially variable with an adjusted *P* value of < 0.01.

Cell type abundance analysis in Stereo-seq data

To test for differential abundance of cell types between age groups, we used mixed effects modelling of associations of single cells (MASC). MASC tests whether cell type membership of individual cells is influenced by an experimental covariate of interest, while accounting for technical covariates and biological variation. We specified mouse genotype as a fixed covariate and mouse of origin as a random effect in the generalized, mixed-effect model. Changes in cell type abundance were considered significant at FDR-$P < 0.01$.

Differential gene expression analysis

Differential gene expression analysis in TRAP samples (including calculation of gene enrichment and depletion, relative to tissue homogenate RNA) was performed using DESeq2 (v1.36.0, RRID:SCR_015687) in R (v4.2.1, RRID:SCR_001905) with Bioconductor (v3.15, RRID:SCR_006442). Adaptive shrinkage of log fold change estimates was performed using ashr. The following settings were changed from defaults: minReplicatesForReplace = Inf, cooksCutoff = Inf, filterFun = ihw, lfcThreshold = $\log_2(1.05)$. Protein-protein interactions were obtained using STRINGdb (version 11) with a minimum confidence threshold of 0.4[56].

Specificity index calculation in TRAP/RiboTag samples

To calculate the specificity index of genes detected within TRAP/RiboTag datasets of dopaminergic neurons and other cell types within midbrain, pSI (v1.1) was used with default settings[20,22,30–32,57]. Genes were considered significantly specifically expressed with an FDR-adjusted *P* value < 0.01.

Differential transcript usage analysis

Differential transcript usage was performed using DRIMSeq (v1.24.0). To consider only genes containing more than 1 isoform, with a minimum level of expression, the following parameters were used: min_samps_gene_expr = n * 0.75, min_gene_expr = 10, min_samps_feature_expr = 10, min_feature_expr = 10, min_samps_feature_prop = 10, min_feature_prop = 0.1.

GWAS prioritization analysis

A list of 303 genes (sourced from Nalls et al., 2019 supplementary materials), containing SNPs at an $r^2 > 0.5$ and located within ±1 Mb of 107 common risk variants for sporadic PD was used for prioritization analysis[35]. To convert between human and mouse gene symbols, homologene (v1.4.68.19.3.27, RRID:SCR_002924) and biomaRt (v2.52.0, RRID:SCR_019214) were used[58,59]. TRAP enrichment (measured as the product of the $\log_2$ fold-change and FDR-adjusted *P* value) and specificity indices for DAT-TRAP samples were used for gene prioritization, per lead SNP.

Gene set enrichment analysis

Gene set enrichment analysis was performed using fgsea (v1.22.0, RRID:SCR_020938) with the following parameters: eps = 0, minSize = 10, maxSize = 500, nPermSimple = 10000. Pathway data were obtained from the Molecular Signatures Database (v7.5.1,

RRID:SCR_016863), using C2 Canonical Pathways from Kegg and C5 Gene Ontology sets[60,61].

Statistics and reproducibility

No statistical methods were used to predetermine sample sizes, but our sample sizes for TRAP analyses surpass those reported in previous publications[21,62,63] and our sample sizes for Stereo-seq samples are comparable with those of similar spatial transcriptomic datasets[9]. All statistical analyses were performed with R (v4.2.1) and Python (v3.9). All *P* values were modified to an FDR of 1 % or 5 % as described in the text with the Benjamini & Hochberg method.

Data and code availability

All raw data from TRAP experiment have been uploaded to the Gene Expression Omnibus (GEO accession number: GSE215276). The Stereo-seq raw data that supports the findings of this study have been deposited into CNGB Sequence Archive (CNSA) of China National GeneBank DataBase (CNGBdb) with accession number CNP0003397. All processed data, including results of all analyses are provided at *spatialbrain.org*. All code for processing data from raw input or processed counts are provided at *https://github.com/peterkilfeather/spatialbrain*. Protocols for laboratory collection and processing of samples as described in this study are published as a collection at protocols.io (DOI: Pending publication).

Authors Contributions

P.K. performed all analyses, with help from J.H.K. and H.L. P.K. and K.W. optimized and performed TRAP experiments. P.K. performed all long-read sequencing experiments, all immunohistochemistry experiments, and all tissue collection for Stereo-seq. M.C.C. performed Fura-2 CASR and iPSC ICC experiments. Y.A., J.H.K., X.Z. and X.C. performed the Stereo-seq experiments. N.C.-R. co-supervised the project and contributed to project and experimental design. R.W.M conceived the project. R.W.M and Z.S. supervised the entire study and secured funding. P.K. and R.W.M. wrote the paper, with contributions from all authors. All authors reviewed the manuscript and approved its submission.

Acknowledgements

This research was funded in part by Aligning Science Across Parkinson's [ASAP-020370] through the Michael J. Fox Foundation for Parkinson's Research (MJFF), in part by the Monument Trust Discovery Award from Parkinson's UK (J-1403), and in part by Science, Technology and Innovation Commission of Shenzhen Municipality under grant No. JCYJ20180507183628543. We sincerely thank the support provided by China National GeneBank.For the purpose of open access, the author has applied a CC BY public copyright license to all Author Accepted Manuscripts arising from this submission. P.K. was supported by a Medical Research Council studentship and post-doctoral Fellowship; K.W. was supported by a Parkinson's UK studentship (H-1301) and M.C.C. was supported by the Joan Pitts-Tucker/Heyman Moritz Studentship.

Supplementary Table 1: Stereo-seq cell type annotation summary, n per cell type

Supplementary Table 2: Spatially variable genes per cell type

Supplementary Table 3: PD GWAS Candidate genes

Figure 1

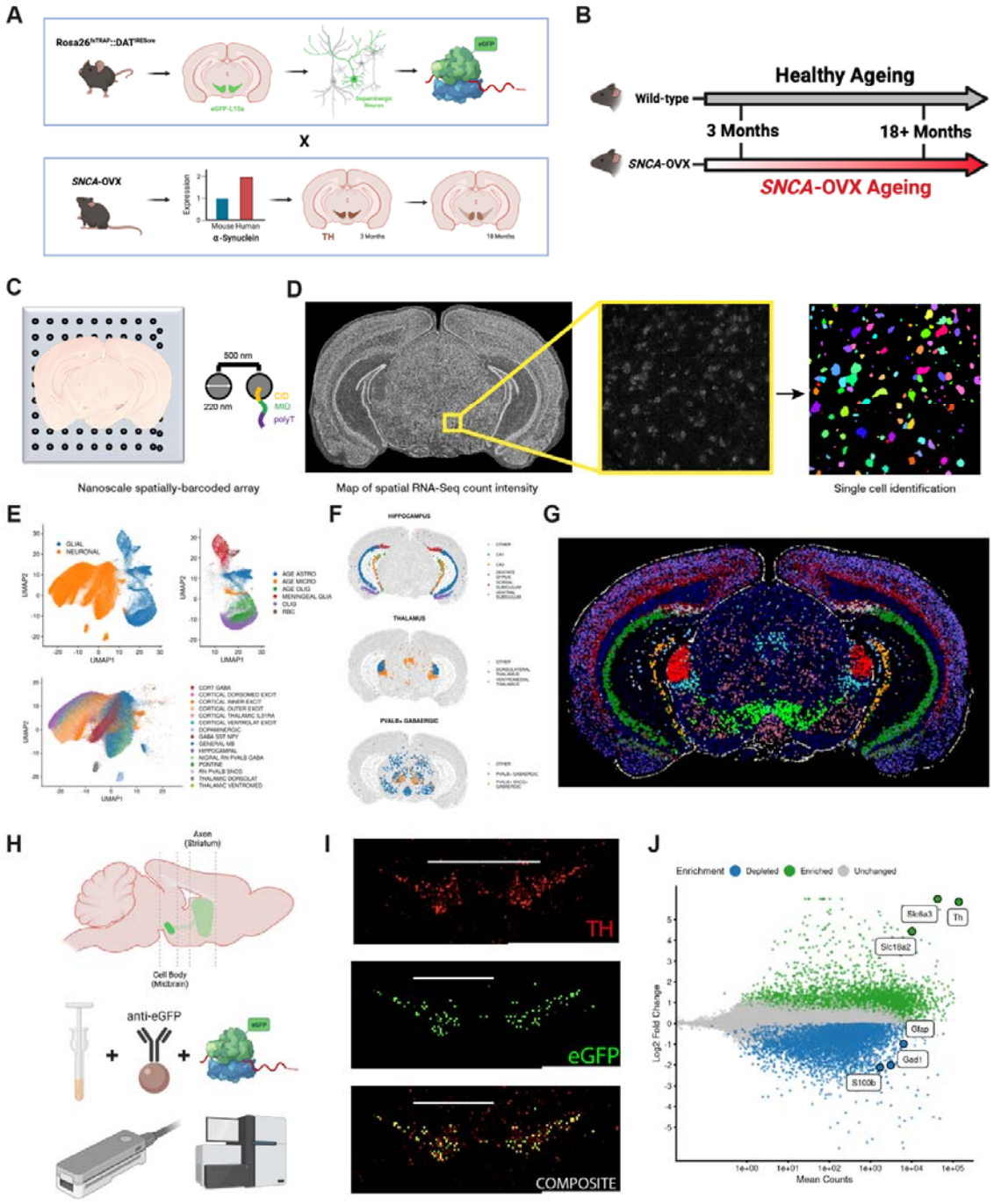
A
Rosa26hTRAP::DATIREScre
eGFP-L10a
eGFP
X
SNCA-OVX
Expression
Mouse Human
α-Synuclein
TH
3 Months
18 Months
B
Healthy Ageing
Wild-type
3 Months
18+ Months
SNCA-OVX
SNCA-OVX Ageing
C
500 nm
220 nm
CID
MID
polyT
Nanoscale spatially-barcoded array
D
Map of spatial RNA-Seq count intensity
Single cell identification
E
GLIAL
NEURONAL
UMAP1
UMAP2
F
HIPPOCAMPUS
THALAMUS
PVALB+ GABAERGIC
G
H
Axon
(Striatum)
Cell Body
(Midbrain)
anti-eGFP
eGFP
I
TH
eGFP
COMPOSITE
J
Enrichment
Depleted
Enriched
Unchanged
Slc6a3
Th
Slc18a2
Gfap
Gad1
S100b
Log2 Fold Change
Mean Counts

Figure 2

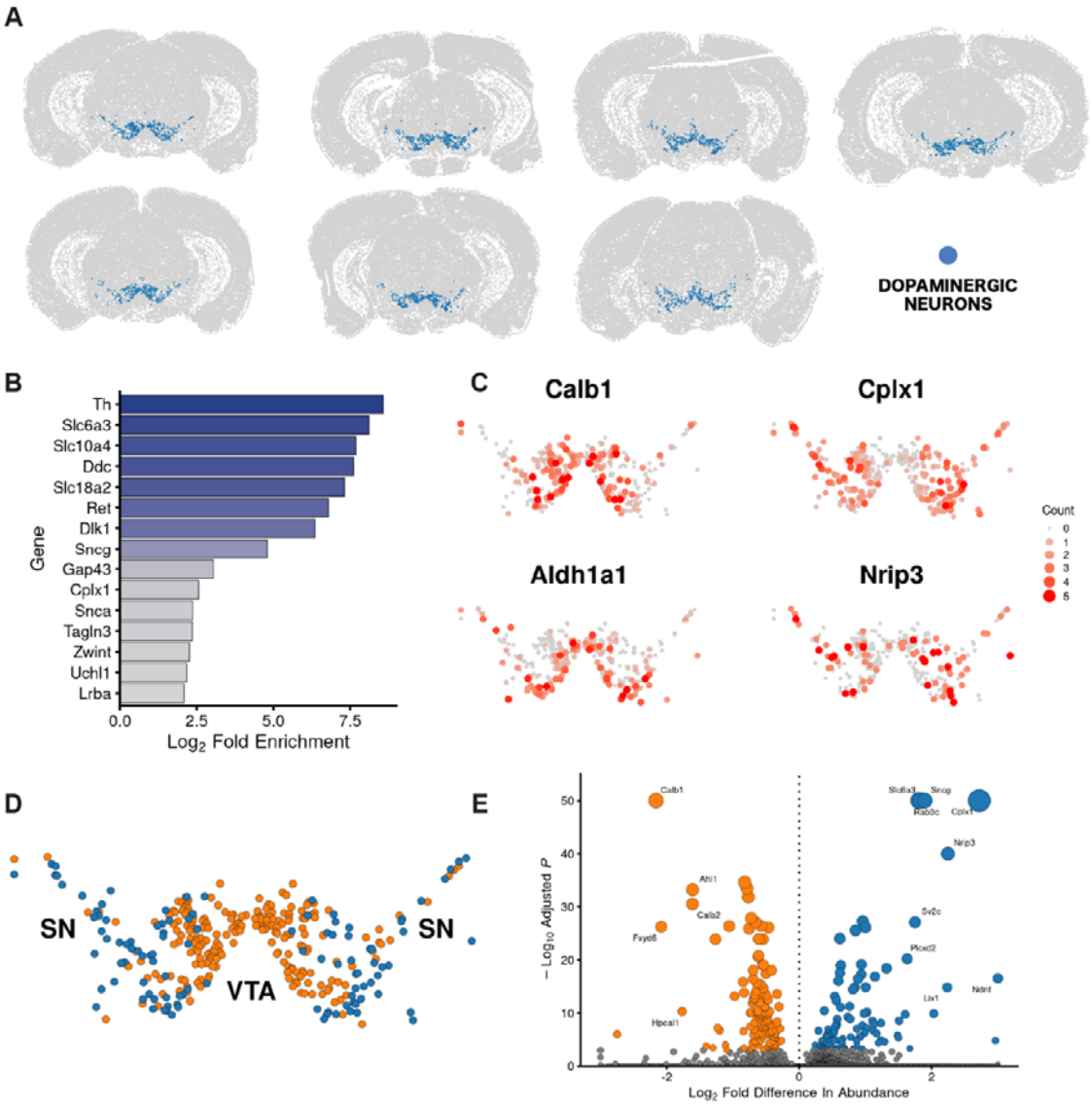
A
DOPAMINERGIC NEURONS
B
Th
Slc6a3
Slc10a4
Ddc
Slc18a2
Ret
Dlk1
Sncg
Gap43
Cplx1
Snca
Tagln3
Zwint
Uchl1
Lrba
Gene
0.0
2.5
5.0
7.5
Log2 Fold Enrichment
C
Calb1
Cplx1
Aldh1a1
Nrip3
Count
0
1
2
3
4
5
D
SN
VTA
SN
E
Calb1
Slc6a3
Sncg
Rab3c
Cplx1
Nrip3
Ahi1
Calb2
Fxyd6
Hpcal1
Sv2c
Plcxd2
Lix1
Ndnf
−Log10 Adjusted P
50
40
30
20
10
0
-2
0
2
Log2 Fold Difference In Abundance

Figure 3

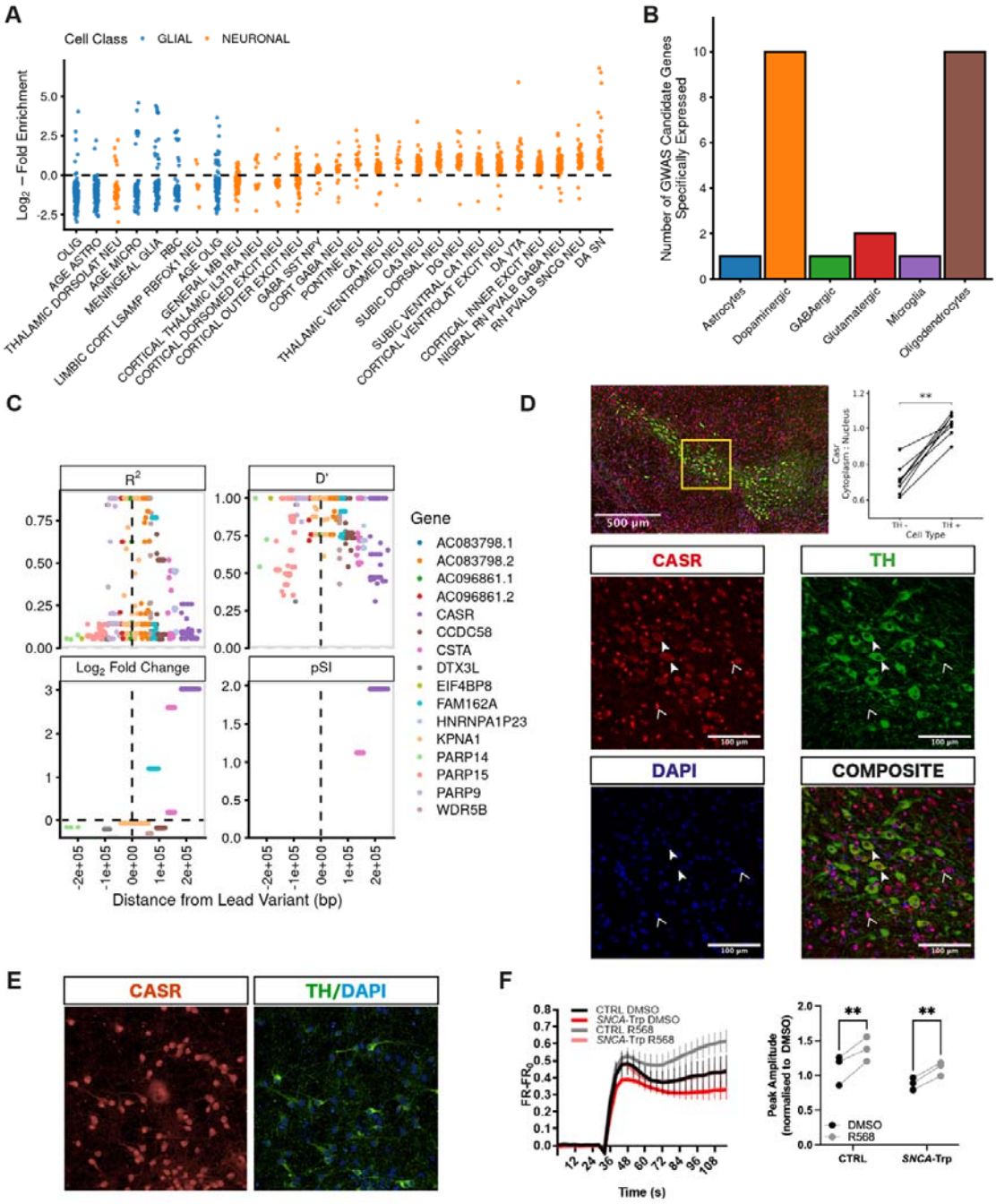
A
Cell Class • GLIAL • NEURONAL
Log2 – Fold Enrichment
OLIG
AGE ASTRO
THALAMIC DORSOLAT NEU
AGE MICRO
MENINGEAL GLIA
RBC
LIMBIC CORT LSAMP RBFOX1 NEU
AGE OLIG
GENERAL MB NEU
CORTICAL THALAMIC IL31RA NEU
CORTICAL DORSOMED EXCIT NEU
CORTICAL OUTER EXCIT NEU
GABA SST NPY
CORT GABA NEU
PONTINE NEU
CA1 NEU
THALAMIC VENTROMED NEU
CA3 NEU
SUBIC DORSAL NEU
DG NEU
SUBIC VENTRAL CA1 NEU
CORTICAL VENTROLAT EXCIT NEU
DA VTA
CORTICAL INNER EXCIT NEU
NIGRAL RN PVALB GABA NEU
RN PVALB SNCG NEU
DA SN
B
Number of GWAS Candidate Genes Specifically Expressed
Astrocytes
Dopaminergic
GABAergic
Glutamatergic
Microglia
Oligodendrocytes
C
R2
D'
Log2 Fold Change
pSI
Gene
AC083798.1
AC083798.2
AC096861.1
AC096861.2
CASR
CCDC58
CSTA
DTX3L
EIF4BP8
FAM162A
HNRNPA1P23
KPNA1
PARP14
PARP15
PARP9
WDR5B
Distance from Lead Variant (bp)
D
500 µm
Casr Cytoplasm : Nucleus
Cell Type
CASR
TH
DAPI
COMPOSITE
E
CASR
TH/DAPI
F
CTRL DMSO
SNCA-Trp DMSO
CTRL R568
SNCA-Trp R568
FR-FR0
Time (s)
Peak Amplitude (normalised to DMSO)
DMSO
R568
CTRL
SNCA-Trp

Figure 4

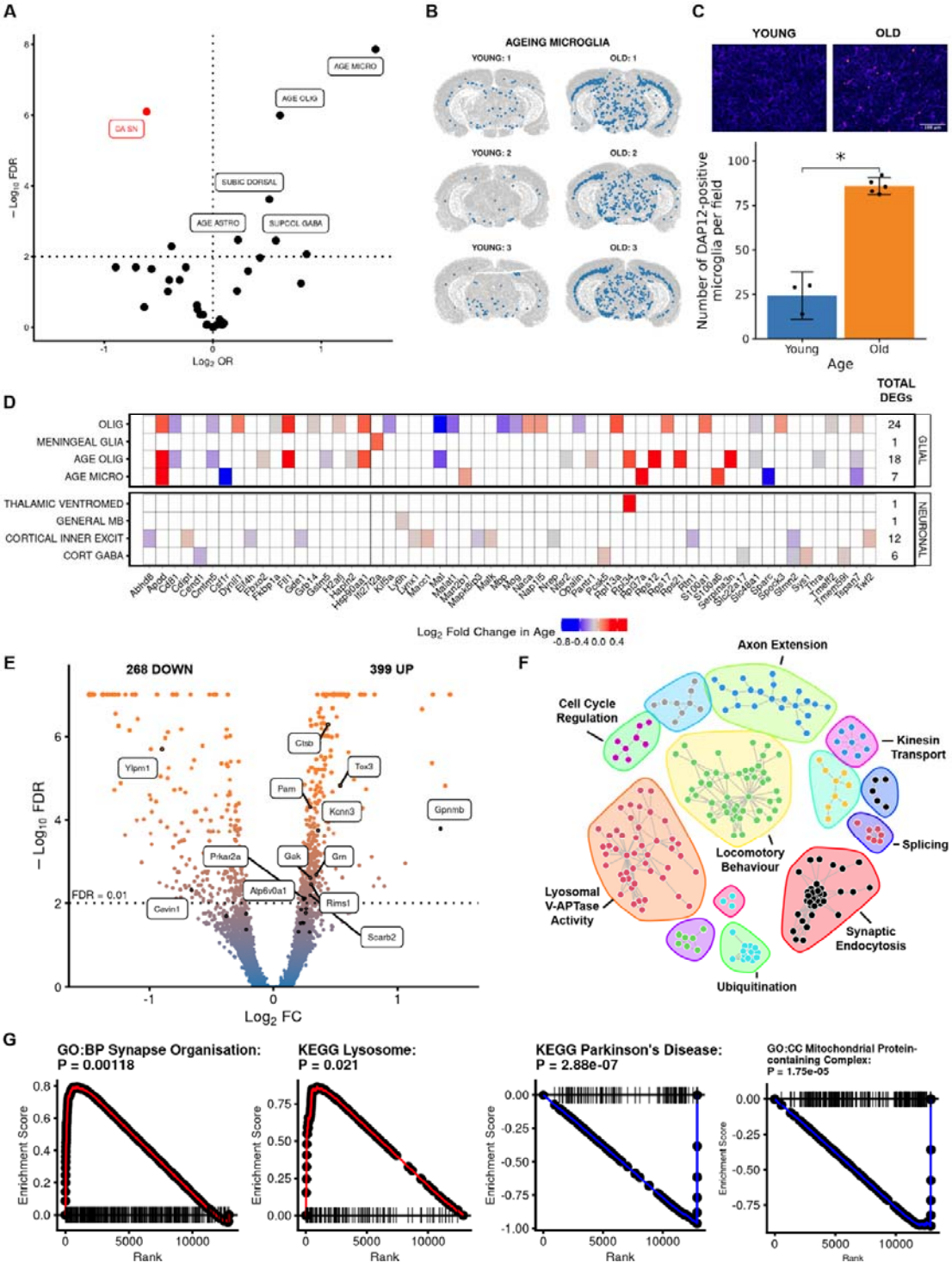
A
AGE MICRO
AGE OLIG
DA SN
SUBIC DORSAL
AGE ASTRO
SUPCOL GABA
− Log10 FDR
Log2 OR
B
AGEING MICROGLIA
YOUNG: 1
OLD: 1
YOUNG: 2
OLD: 2
YOUNG: 3
OLD: 3
C
YOUNG
OLD
Number of DAP12-positive microglia per field
Young
Old
Age
D
TOTAL DEGs
OLIG
MENINGEAL GLIA
AGE OLIG
AGE MICRO
THALAMIC VENTROMED
GENERAL MB
CORTICAL INNER EXCIT
CORT GABA
GLIAL
NEURONAL
Log2 Fold Change in Age
E
268 DOWN
399 UP
Ylpm1
Ctsb
Tox3
Pam
Kcnn3
Gpnmb
Prkar2a
Gak
Grn
Atp6v0a1
Rims1
Cevin1
Scarb2
FDR = 0.01
− Log10 FDR
Log2 FC
F
Axon Extension
Cell Cycle Regulation
Kinesin Transport
Splicing
Locomotory Behaviour
Lyosomal V-APTase Activity
Synaptic Endocytosis
Ubiquitination
G
GO:BP Synapse Organisation: P = 0.00118
KEGG Lysosome: P = 0.021
KEGG Parkinson's Disease: P = 2.88e-07
GO:CC Mitochondrial Protein-containing Complex: P = 1.75e-05
Enrichment Score
Rank

Supplementary Figure 1

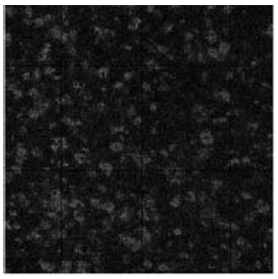

1. Total Counts per XY Position

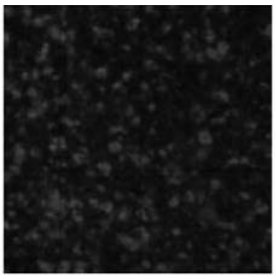

2. Gaussian Filter (Sigma = 5)

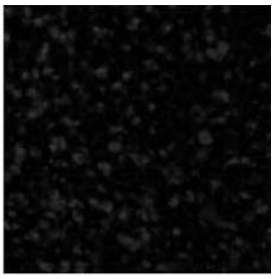

3. Background Subtraction (Rolling Ball - 100 px)

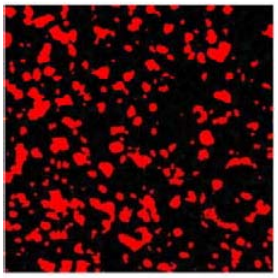

4. Iterative Intermeans Thresholding

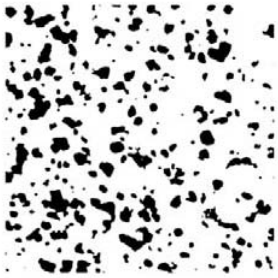

5. Conversion to Mask

6. Fill Holes

7. Watershed

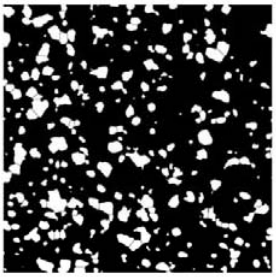

8. Invert LUT

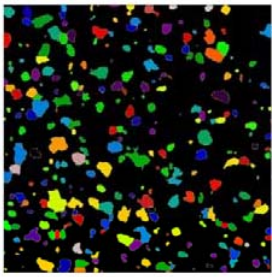

9. Label Cells

Cell	Gene	Count
65	Th	18
15	Th	26
77	Th	77
46	Th	36
47	Slc6a3	33
37	Slc6a3	49
50	Slc6a3	20
47	Slc6a3	68
35	Slc18a2	13
4	Slc18a2	20
35	Slc18a2	50
62	Slc18a2	76

10. Aggregate counts per gene per cell

Supplementary Figure 2

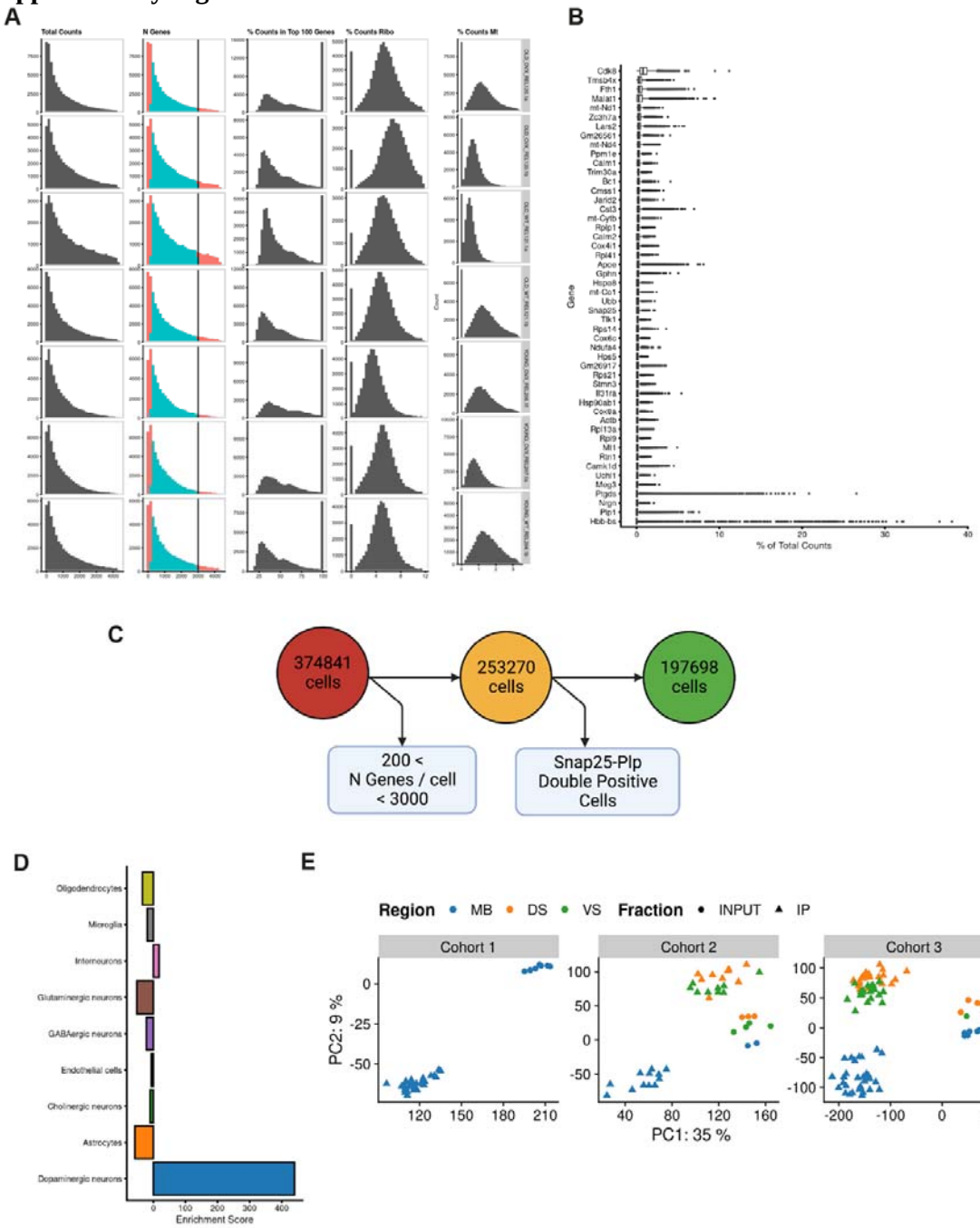

Supplementary Figure 3

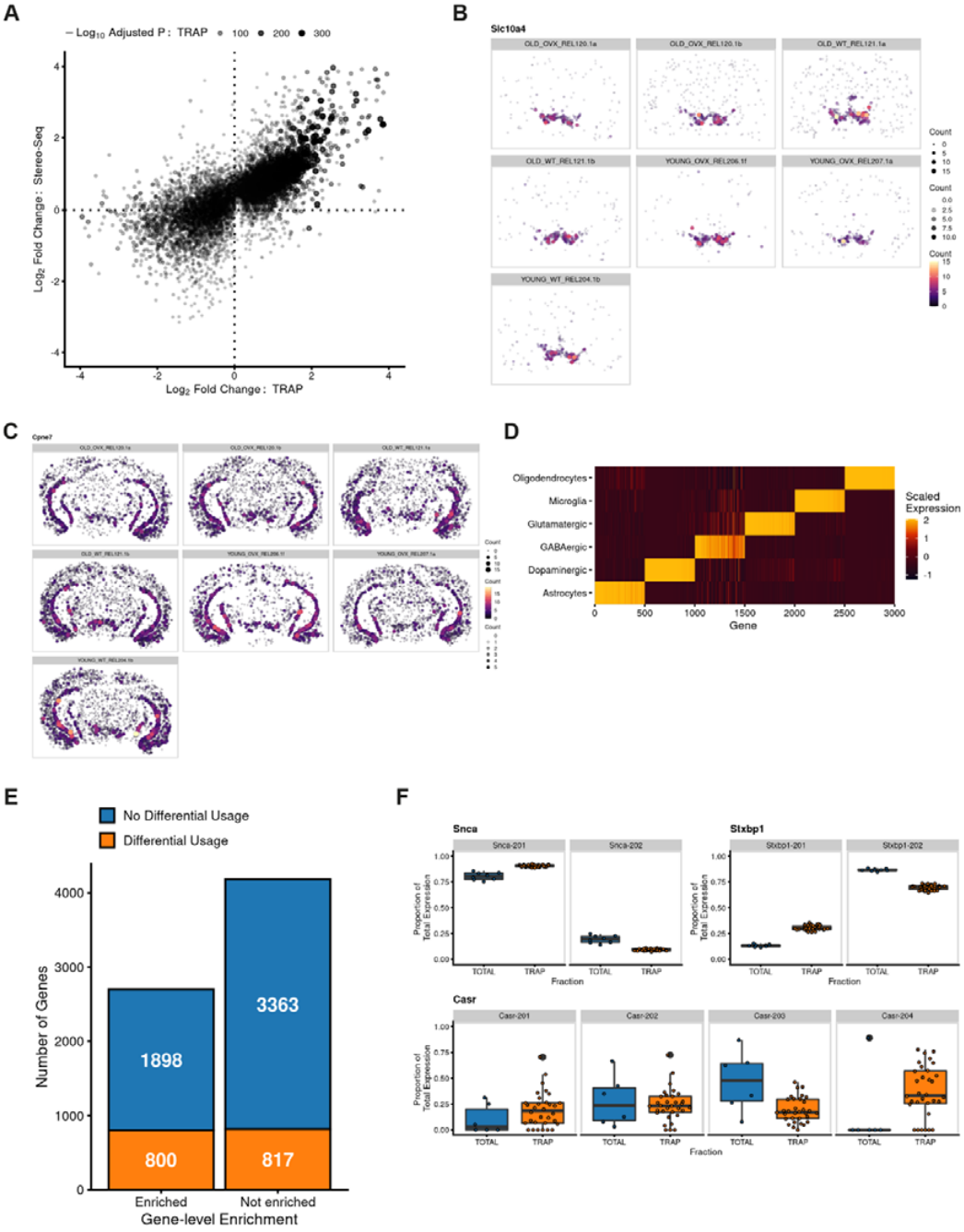

Supplementary Figure 4

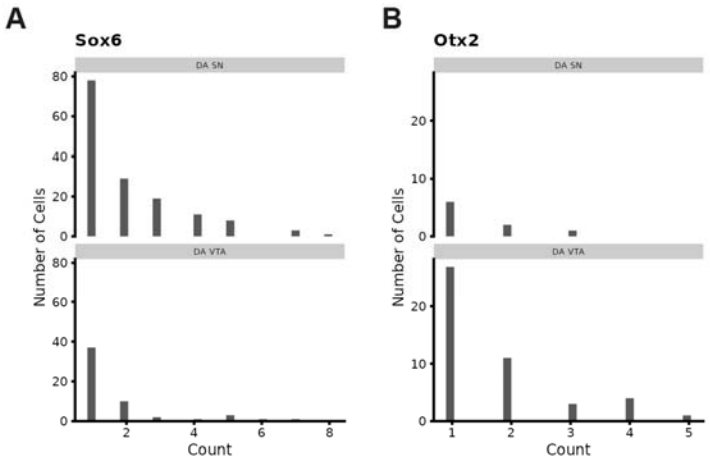

Supplementary Figure 5

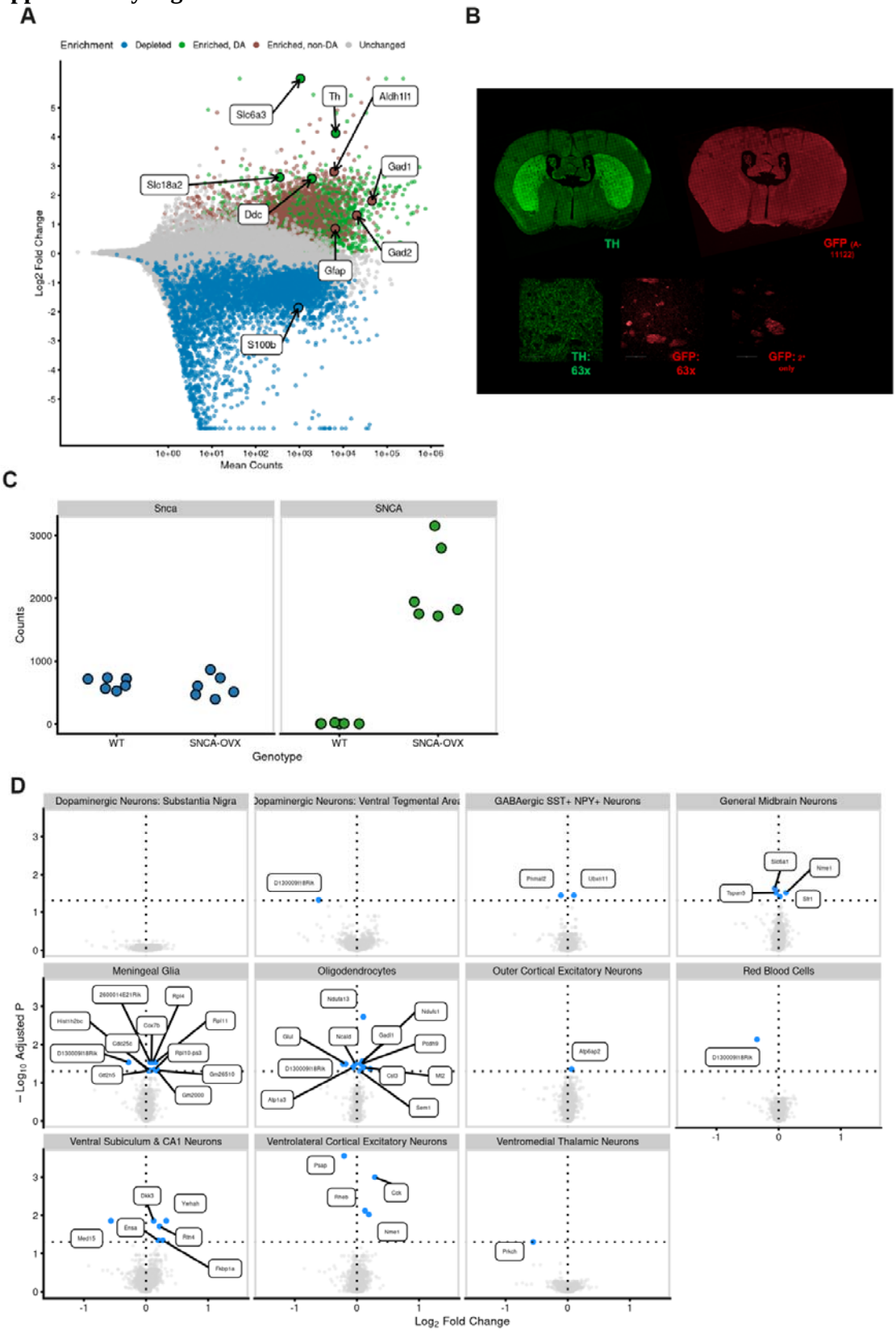

Figure legends

Figure 1: Integration of Stereo-seq and TRAP for high resolution gene expression profiling. A) Transgenic mouse model: Rosa26^{fsTRAP}::DAT^{IREScre} mice were crossed with *SNCA*-OVX mice to enable the capture of dopaminergic mRNA in a model of PD. B) Mice were aged to 18+ months in order to study the effect of healthy and Parkinsonian ageing. C) Stereo-seq array, with spatial transcript map from a single brain section. D) Conversion of transcript expression map to segmented individual cells. Segmented cells were subsequently filtered on the basis of transcriptome size and complexity. E) Uniform Manifold Approximation Projection (UMAP) of 197,698 cells divided into neuronal and glial cell types. F and G) Demonstration of spatial compartmentalization of annotated cell types: Spatially distinct populations of the hippocampus, thalamus, cortex and midbrain nuclei can be visualized. H) Dissection and TRAP processing schematic, before performing short- and long-read RNA sequencing. eGFP-tagged ribosomes in DAT-expressing cells are captured by anti-GFP antibody-coated paramagnetic beads. I) Confirmation of eGFP colocalization with tyrosine hydroxylase (TH), a marker of dopaminergic neurons. J) Demonstration of the specific enrichment of dopaminergic marker genes and depletion of marker genes of other neighboring cell types in DAT-TRAP mRNA (n = 76).

Figure 1: High resolution single cell spatial mapping of sub-populations of DA neurons. A) Confirmation of the spatial distribution of cells annotated as dopaminergic neurons. B) Top marker genes of dopaminergic neurons identified from Stereo-seq data, including less commonly recognised *Slc10a4*, *Gap43*, *Cpne7*. C) Examples of spatially variably expressed genes, recapitulating SN-VTA compartmentalization. D) Unsupervised clustering demonstrating the presence of two distinct clusters, reflecting the SN and VTA. E) Volcano plot highlighting the marker genes of SN and VTA populations (n = 7 brains, 2322 cells for all analyses).

Figure 2: Mapping, expression, and function of PD GWAS risk loci. A) Log_2-fold enrichment or depletion of candidate PD GWAS genes in each annotated cell type from Stereo-seq data. Genes were, with exceptions, generally enriched in neurons and depleted in glia. B) The number of candidate PD GWAS genes found to be significantly specifically expressed in each TRAP/RiboTag cell type tested. Dopaminergic neurons and Oligodendrocytes jointly specifically expressed the greatest number of candidate genes (n = 72 (DAT-TRAP samples), 6 (GABAergic neurons), 6 (Glutamatergic neurons), 3 (Oligodendrocytes), 6 (Microglia), 6 (Astrocytes)). C) Linkage disequilibrium measures (R^2 and D') for rs55961674, indicating the candidacy of > 8 genes for consideration. CASR was the most enriched and specifically expressed candidate gene. D) Immunohistochemical confirmation of specific Casr expression in TH-positive cytoplasm of the mouse ventral midbrain (filled arrows). Casr could be detected in neighboring nuclei of TH-negative cells (open arrows). The cytoplasm:nucleus ratio of Casr signal was significantly greater in TH-positive cells; paired wilcoxon rank sum text, (n = 8, P = 0.0078). E) Immunocytochemical confirmation of CASR expression in TH-positive induced pluripotent stem cell-derived dopaminergic neurons. F) Confirmation of CASR-mediated regulation of intracellular Ca^{2+} handling: R568 (a positive allosteric modulator of CASR) increased the Fura2 peak amplitude response to ionomycin administration (n = 3 per genotype; 2 genotypes; two-way repeated measures analysis of variance (ANOVA) by treatment group and genotype; F = 92.8, P = 0.0006).

Figure 3: High resolution age-related changes in gene expression. A) Odds ratio analysis of cell type abundance with ageing in Stereo-seq annotated cell types. Substantia nigra dopaminergic neurons were significantly depleted in aged brains, while activated microglia and oligodendrocytes were detected in greater number. B) The expansion of activated microglia was observed in midbrain, corpus callosum and the external capsule. C)

Confirmatory immunohistochemical staining for Tyrobp/Dap12, the leading transcriptomic marker of this cell population confirmed an increase microglial count in aged brain sections. Wilcoxon rank sum test, (n = 3 (Young brains), 5 (Old brains), P = 0.036, data here are represented as the mean ± 99 % confidence interval). Representative fields from young and old midbrain sections stained for Tyrobp/Dap12 presented above (Methods). D) Heatmap of glial and neuronal ageing expression changes detected in Stereo-seq samples. Glial cell types demonstrated a more marker expression change. E) Volcano plot of the fold change and FDR of genes comparing aged and young TRAP samples (n = 56). 13 candidate PD GWAS genes were within the genes significantly differentially expressed. F) Protein-protein interactions among TRAP-differentially expressed genes were used to identify functionally distinct clusters. G) Gene set enrichment analysis identifies and confirms the up- or downregulation of pathways relevant to ageing in dopaminergic neurons.

Supplementary Figure 1: Stereo-seq segmentation pipeline

1. A transcript "map" was generated by calculating the total number of counts detected per spatial X-Y position across all genes. 2. Gaussian filtering (sigma = 5) to enhance signal from cell regions and reduce signal from the background. 3. Rolling ball background subtraction to further remove background signal. 4 – 5. Iterative means thresholding followed by conversion to a binary mask. 6. "Holes" were filled to improve the masking of cellular regions with lower signal. 7. Watershed to segment each masked region into distinct objects. 8 – 9. Inversion of the binary mask and object labelling. 10. Aggregation of gene counts to the cell-level.

Supplementary Figure 2: Stereo-seq and TRAP quality control

A) Histograms of the total counts, number of genes detected, % of counts assigned to the top 100 most expressed genes, % of counts assigned to ribosomal genes and % of counts assigned to mitochondrial genes per brain. Cells were filtered to exclude those containing fewer than

200 and greater than 3000 genes each. B) % of total counts assigned to the top 50 expressed genes across the entire dataset. C) The number of cells retained at each filtering step. During unsupervised clustering, a subset of cells contained both neuronal and glial markers (e.g. Snap25/Plp1). These cells were excluded from further analysis, as their identity could not be confirmed. D) Enrichment score ($-\log_{10} P$ multiplied by $\log_2$ fold-change) for cell types likely to be resident within dissected midbrain tissue for TRAP. DA neurons were the only cell type, out of 178 that showed clear enrichment. E) Principal component analysis (PCA) biplot of TRAP samples. TRAP samples were collected in three cohorts, as shown. Samples were most clearly distinguished along PC1 and PC2 by the effect of TRAP capture, separating TRAP and 'Input' homogenate samples and by the region of origin (MB, midbrain; DS, dorsal striatum; VS, ventral striatum).

Supplementary Figure 3: Specificity analysis of TRAP/RiboTag datasets and DA splicing summary

A) Log_2 fold-change of genes detected in TRAP and Stereo-seq datasets between old and young samples. The concordance between both technologies is illustrated by the predominance of genes in the bottom left and top right quadrants. B and C) Examples of Slc10a4 and Cpne7 demonstrating DA neuron enrichment in Stereo-seq brain sections. D) Scaled expression heatmap of the top 500 per cell type that are specifically expressed in each TRAP/RiboTag dataset. E) Summary of the number of the genes found to exhibit differential transcript usage in midbrain TRAP samples, relative to midbrain homogenate RNA. Differential transcript usage is evident to an equal degree in genes enriched and not enriched by TRAP. F) Example of differential transcript usage of *Snca*, *Stxbp1*, *Casr* in midbrain TRAP samples.

Supplementary Figure 4: Sox6 and Otx2 counts in each Stereo-seq cell type

A and B) Histograms of Sox6 and Otx2 expression. Sox6 was detected in greater abundance in substantia nigra, while Otx2 was detected in greater abundance in ventral tegmental area DA neurons. Counts represent raw counts.

Supplementary Figure 5: Investigating axonal translation in DA neurons and SNCA-OVX Characterization in TRAP and Stereo-seq samples

A) MA plot of enrichment/depletion in striatal TRAP samples. Markers of DA neurons (e.g. *Th, Slc6a3 (DAT), Slc18a2 (VMAT2)*) were enriched by TRAP, however markers of other cell types (e.g. *Gfap, Gad1*) were also enriched (*n* = 62 DAT-TRAP mRNA, n = 23 striatal homogenate mRNA). B) Immunohistochemical staining for GFP and TH in mouse striatum revealed the presence of faint puncta that colocalize with TH. C) Confirmation of *SNCA* overexpression specifically in *SNCA*-OVX samples (*n* = 12). *Snca* expression is unaffected by *SNCA* overexpression. Counts represent DESeq2-normalized read counts per sample. D) Volcano plots for all genes significantly differentially expressed due to *SNCA* overexpression across cell types of Stereo-seq samples.

References

1. Dickson, D. W. *et al.* Neuropathological assessment of Parkinson's disease: refining the diagnostic criteria. *Lancet Neurol.* **8**, 1150–1157 (2009).
2. Halliday, G. M., Holton, J. L., Revesz, T. & Dickson, D. W. Neuropathology underlying clinical variability in patients with synucleinopathies. *Acta Neuropathol. (Berl.)* **122**, 187–204 (2011).
3. de Lau, L. M. & Breteler, M. M. Epidemiology of Parkinson's disease. *Lancet Neurol.* **5**, 525–535 (2006).
4. Fearnley, J. M. & Lees, A. J. Ageing and Parkinson's disease: substantia nigra regional selectivity. *Brain J. Neurol.* **114 (Pt 5)**, 2283–2301 (1991).
5. McGeer, P. L., McGeer, E. G. & Suzuki, J. S. Aging and Extrapyramidal Function. *Arch. Neurol.* **34**, 33–35 (1977).
6. Janezic, S. *et al.* Deficits in dopaminergic transmission precede neuron loss and dysfunction in a new Parkinson model. *Proc. Natl. Acad. Sci. U. S. A.* **110**, E4016-4025 (2013).
7. Hunn, B. H. M. *et al.* Impairment of Macroautophagy in Dopamine Neurons Has Opposing Effects on Parkinsonian Pathology and Behavior. *Cell Rep.* **29**, 920-931.e7 (2019).
8. Ximerakis, M. *et al.* Single-cell transcriptomic profiling of the aging mouse brain. *Nat. Neurosci.* **22**, 1696–1708 (2019).
9. Kamath, T. *et al.* Single-cell genomic profiling of human dopamine neurons identifies a population that selectively degenerates in Parkinson's disease. *Nat. Neurosci.* **25**, 588–595 (2022).

10. Zeisel, A. *et al.* Cell types in the mouse cortex and hippocampus revealed by single-cell RNA-seq. *Science* **347**, 1138–1142 (2015).
11. La Manno, G. *et al.* Molecular Diversity of Midbrain Development in Mouse, Human, and Stem Cells. *Cell* **167**, 566-580.e19 (2016).
12. Poulin, J.-F., Gaertner, Z., Moreno-Ramos, O. A. & Awatramani, R. Classification of Midbrain Dopamine Neurons Using Single-Cell Gene Expression Profiling Approaches. *Trends Neurosci.* **43**, 155–169 (2020).
13. Poulin, J.-F. *et al.* Defining Midbrain Dopaminergic Neuron Diversity by Single-Cell Gene Expression Profiling. *Cell Rep.* **9**, 930–943 (2014).
14. van den Brink, S. C. *et al.* Single-cell sequencing reveals dissociation-induced gene expression in tissue subpopulations. *Nat. Methods* **14**, 935–936 (2017).
15. Moses, L. & Pachter, L. Museum of spatial transcriptomics. *Nat. Methods* **19**, 534–546 (2022).
16. Chen, A. *et al.* Spatiotemporal transcriptomic atlas of mouse organogenesis using DNA nanoball-patterned arrays. *Cell* **185**, 1777-1792.e21 (2022).
17. Svensson, V. *et al.* Power Analysis of Single Cell RNA-Sequencing Experiments. *Nat. Methods* **14**, 381–387 (2017).
18. Heiman, M., Kulicke, R., Fenster, R. J., Greengard, P. & Heintz, N. Cell type–specific mRNA purification by translating ribosome affinity purification (TRAP). *Nat. Protoc.* **9**, 1282–1291 (2014).
19. Dougherty, J. D. *et al.* Candidate pathways for promoting differentiation or quiescence of oligodendrocyte progenitor-like cells in glioma. *Cancer Res.* **72**, 4856–4868 (2012).

20. Dougherty, J. D. *et al.* The disruption of Celf6, a gene identified by translational profiling of serotonergic neurons, results in autism-related behaviors. *J. Neurosci. Off. J. Soc. Neurosci.* **33**, 2732–2753 (2013).
21. Doyle, J. P. *et al.* Application of a translational profiling approach for the comparative analysis of CNS cell types. *Cell* **135**, 749–762 (2008).
22. Sakers, K. *et al.* Astrocytes locally translate transcripts in their peripheral processes. *Proc. Natl. Acad. Sci.* **114**, E3830–E3838 (2017).
23. Shigeoka, T. *et al.* Dynamic Axonal Translation in Developing and Mature Visual Circuits. *Cell* **166**, 181–192 (2016).
24. Hobson, B. D. *et al.* Subcellular and regional localization of mRNA translation in midbrain dopamine neurons. *Cell Rep.* **38**, 110208 (2022).
25. Blevins, W. R. *et al.* Extensive post-transcriptional buffering of gene expression in the response to severe oxidative stress in baker's yeast. *Sci. Rep.* **9**, 11005 (2019).
26. Zhou, P. *et al.* Interrogating translational efficiency and lineage-specific transcriptomes using ribosome affinity purification. *Proc. Natl. Acad. Sci.* **110**, 15395–15400 (2013).
27. Bäckman, C. M. *et al.* Characterization of a mouse strain expressing Cre recombinase from the 3' untranslated region of the dopamine transporter locus. *Genes. N. Y. N 2000* **44**, 383–390 (2006).
28. Larhammar, M. *et al.* SLC10A4 Is a Vesicular Amine-Associated Transporter Modulating Dopamine Homeostasis. *Biol. Psychiatry* **77**, 526–536 (2015).
29. Park, Y.-H. *et al.* CPNE7-Induced Autophagy Restores the Physiological Function of Mature Odontoblasts. *Front. Cell Dev. Biol.* **9**, (2021).
30. Paul, E. J., Tossell, K. & Ungless, M. A. Transcriptional profiling aligned with in situ expression image analysis reveals mosaically expressed molecular markers for GABA

neuron sub-groups in the ventral tegmental area. *Eur. J. Neurosci.* **50**, 3732–3749 (2019).

31. Voskuhl, R. R. *et al.* Gene expression in oligodendrocytes during remyelination reveals cholesterol homeostasis as a therapeutic target in multiple sclerosis. *Proc. Natl. Acad. Sci.* **116**, 10130–10139 (2019).
32. Ouwenga, R., Lake, A. M., Aryal, S., Lagunas, T. & Dougherty, J. D. The Differences in Local Translatome across Distinct Neuron Types Is Mediated by Both Baseline Cellular Differences and Post-transcriptional Mechanisms. *eNeuro* **5**, ENEURO.0320-18.2018 (2018).
33. Finucane, H. K. *et al.* Heritability enrichment of specifically expressed genes identifies disease-relevant tissues and cell types. *Nat. Genet.* **50**, 621–629 (2018).
34. Hook, P. W. *et al.* Single-Cell RNA-Seq of Mouse Dopaminergic Neurons Informs Candidate Gene Selection for Sporadic Parkinson Disease. *Am. J. Hum. Genet.* **102**, 427–446 (2018).
35. Nalls, M. A. *et al.* Identification of novel risk loci, causal insights, and heritable risk for Parkinson's disease: a meta-analysis of genome-wide association studies. *Lancet Neurol.* **18**, 1091–1102 (2019).
36. Reynolds, R. H. *et al.* Moving beyond neurons: the role of cell type-specific gene regulation in Parkinson's disease heritability. *Npj Park. Dis.* **5**, 1–14 (2019).
37. Fox, J., Lowe, S. H., Petty, B. A. & Nemeth, E. F. NPS R-568: a type II calcimimetic compound that acts on parathyroid cell calcium receptor of rats to reduce plasma levels of parathyroid hormone and calcium. *J. Pharmacol. Exp. Ther.* **290**, 473–479 (1999).
38. Grynkiewicz, G., Poenie, M. & Tsien, R. Y. A new generation of Ca2+ indicators with greatly improved fluorescence properties. *J. Biol. Chem.* **260**, 3440–3450 (1985).

39. What is the spatial resolution and configuration of the capture area of the Visium Gene Expression Slide? *10X Genomics* https://kb.10xgenomics.com/hc/en-us/articles/360035487572-What-is-the-spatial-resolution-and-configuration-of-the-capture-area-of-the-Visium-Gene-Expression-Slide-.
40. Rodriques, S. G. *et al.* Slide-seq: A scalable technology for measuring genome-wide expression at high spatial resolution. *Science* **363**, 1463–1467 (2019).
41. Stickels, R. R. *et al.* Highly sensitive spatial transcriptomics at near-cellular resolution with Slide-seqV2. *Nat. Biotechnol.* **39**, 313–319 (2021).
42. Grabert, K. *et al.* Microglial brain region−dependent diversity and selective regional sensitivities to aging. *Nat. Neurosci.* **19**, 504–516 (2016).
43. Salas, I. H., Burgado, J. & Allen, N. J. Glia: victims or villains of the aging brain? *Neurobiol. Dis.* **143**, 105008 (2020).
44. Tansey, M. G. *et al.* Inflammation and immune dysfunction in Parkinson disease. *Nat. Rev. Immunol.* **22**, 657–673 (2022).
45. Papathanou, M., Dumas, S., Pettersson, H., Olson, L. & Wallén-Mackenzie, Å. Off-Target Effects in Transgenic Mice: Characterization of Dopamine Transporter (DAT)-Cre Transgenic Mouse Lines Exposes Multiple Non-Dopaminergic Neuronal Clusters Available for Selective Targeting within Limbic Neurocircuitry. *eNeuro* **6**, ENEURO.0198-19.2019 (2019).
46. Risso, D., Perraudeau, F., Gribkova, S., Dudoit, S. & Vert, J.-P. A general and flexible method for signal extraction from single-cell RNA-seq data. *Nat. Commun.* **9**, 284 (2018).
47. Van den Berge, K. *et al.* Observation weights unlock bulk RNA-seq tools for zero inflation and single-cell applications. *Genome Biol.* **19**, 24 (2018).

48. Larsson, L., Frisén, J. & Lundeberg, J. Spatially resolved transcriptomics adds a new dimension to genomics. *Nat. Methods* **18**, 15–18 (2021).

49. Li, H. Minimap2: pairwise alignment for nucleotide sequences. *Bioinformatics* **34**, 3094–3100 (2018).

50. Patro, R., Duggal, G., Love, M. I., Irizarry, R. A. & Kingsford, C. Salmon provides fast and bias-aware quantification of transcript expression. *Nat. Methods* **14**, 417–419 (2017).

51. Stirling, D. R. *et al.* CellProfiler 4: improvements in speed, utility and usability. *BMC Bioinformatics* **22**, 433 (2021).

52. Wolf, F. A., Angerer, P. & Theis, F. J. SCANPY: large-scale single-cell gene expression data analysis. *Genome Biol.* **19**, 15 (2018).

53. atarashansky. SCTransformPy. (2022).

54. Traag, V. A., Waltman, L. & van Eck, N. J. From Louvain to Leiden: guaranteeing well-connected communities. *Sci. Rep.* **9**, 5233 (2019).

55. Caglayan, E., Liu, Y. & Konopka, G. Ambient RNA analysis reveals misinterpreted and masked cell types in brain single-nuclei datasets. 2022.03.09.483658 Preprint at https://doi.org/10.1101/2022.03.09.483658 (2022).

56. Andrea Franceschini <Andrea. Franceschini@Isb-Sib.Ch>. STRINGdb. (2017) doi:10.18129/B9.BIOC.STRINGDB.

57. Dougherty, J. D., Schmidt, E. F., Nakajima, M. & Heintz, N. Analytical approaches to RNA profiling data for the identification of genes enriched in specific cells. *Nucleic Acids Res.* **38**, 4218–4230 (2010).

58. Mancarci, O. *homologene: Quick Access to Homologene and Gene Annotation Updates*. (2019).

59. Durinck, S., Spellman, P. T., Birney, E. & Huber, W. Mapping identifiers for the integration of genomic datasets with the R/Bioconductor package biomaRt. *Nat. Protoc.* **4**, 1184–1191 (2009).

60. Kanehisa, M. & Goto, S. KEGG: kyoto encyclopedia of genes and genomes. *Nucleic Acids Res.* **28**, 27–30 (2000).

61. The Gene Ontology Consortium *et al.* The Gene Ontology resource: enriching a GOld mine. *Nucleic Acids Res.* **49**, D325–D334 (2021).

62. Brichta, L. *et al.* Identification of neurodegenerative factors using translatome-regulatory network analysis. *Nat. Neurosci.* **18**, 1325–1333 (2015).

63. Nectow, A. R. *et al.* Rapid Molecular Profiling of Defined Cell Types Using Viral TRAP. *Cell Rep.* **19**, 655–667 (2017).